ELECTROCHEMISTRY

LiH formation and its impact on Li batteries revealed by cryogenic electron microscopy

Rafael A. Vilá[1], David T. Boyle[2], Alan Dai[3], Wenbo Zhang[1], Philaphon Sayavong[2], Yusheng Ye[1], Yufei Yang[1], Jennifer A. Dionne[1], Yi Cui[1,4]*

Little is known about how evolved hydrogen affects the cycling of Li batteries. Hypotheses include the formation of LiH in the solid-electrolyte interphase (SEI) and dendritic growth of LiH. Here, we discover that LiH formation in Li batteries likely follows a different pathway: Hydrogen evolved during cycling reacts to nucleate and grow LiH within already deposited Li metal, consuming active Li. We provide the evidence that LiH formed in Li batteries electrically isolates active Li from the current collector that degrades battery capacity. We detect the coexistence of Li metal and LiH also on graphite and silicon anodes, showing that LiH forms in most Li battery anode chemistries. Last, we find that LiH has its own SEI layer that is chemically and structurally distinct from the SEI on Li metal. Our results highlight the formation mechanism and chemical origins of LiH, providing critical insight into how to prevent its formation.

INTRODUCTION

During cycling of Li-ion and Li metal batteries, irreversible reactions, morphological changes, and loss of electroactive materials degrade battery capacity (*1*, *2*). Buildup of gaseous side products in Li batteries is believed to cause failure through cell swelling and rupture, which can sometimes be catastrophic given the flammable nature of evolved gases (*3*, *4*). One concerning side product is hydrogen gas, which evolves during the reduction of water impurities and protic solvent species (*5*). However, before the point of failure, little is known about how hydrogen affects the cycling of Li batteries. Hypotheses for the role of hydrogen include the formation of LiH in the solid-electrolyte interphase (SEI) (*6*) and the dendritic growth of LiH (*7*).

The existence of LiH in Li batteries, its formation mechanism, and the consequences for battery performance remains a poorly understood topic. Aurbach and Weissman (*8*) first commented on the possibility that hydrogen could react at the anode of Li batteries to form LiH. While the reaction between Li metal and hydrogen has a negative standard Gibbs free energy of formation, bulk synthesis by this reaction typically requires high temperatures (>600°C) and pressures of hydrogen to proceed to completion (*9*). The high required temperature has been ascribed to sluggish kinetics that limits the reaction to the surface of Li metal at room temperature. However, the atomic origin of this kinetic barrier remains poorly understood. Given the high temperatures and pressures of hydrogen required for bulk synthesis of LiH and its strong reductive nature (due to the negatively charged hydrogen), the possibility of LiH formation in Li batteries was long overlooked and even dismissed as a possible reaction product (*10*). In 2018, Zachman *et al.* (*7*) identified both Li and LiH on a cycled Li metal foil using electron energy loss spectroscopy (EELS) to measure H and Li K-edges. They claimed that Li metal grows into a low curvature morphology, while LiH electrodeposits as tortuous dendrites, proposing that LiH occurs more frequently than Li metal in commercial carbonate electrolytes. This "dendrite mode" of LiH was hypothesized to lead to capacity loss through mechanical fracture given the poor ductility of LiH. In 2021, Shadike *et al.* (*6*) performed x-ray diffraction (XRD) on the residual SEI of cycled Li metal anodes and identified crystalline LiH, proposing an "SEI mode" for LiH. Given that the SEI is in contact with the electrolyte, the proposed SEI mode of LiH is unexpected because LiH would likely react with the electrolyte because of its reductive properties (*11*).

Given the unfavorable reaction conditions (*9*), few reports of LiH in Li batteries (*6*, *7*, *12*, *13*) and some reports dismissing the existence, it remains uncertain whether LiH occurs in Li batteries, including Li-ion and Li metal batteries. Furthermore, if LiH is formed in Li batteries, it is not clear whether LiH is a beneficial SEI component that promotes reversibility or whether it is a major capacity loss mechanism. In either case, a convincing mechanism for how LiH forms in Li batteries has not been proposed, and its chemical origins remain an open question. Understanding this unexpected result, to either prevent or promote its formation, could provide an additional approach to improve Li batteries beyond their current limitations. In this letter, we combine crystallographic, spectroscopic, and electrochemical techniques at multiple length scales to explore the existence of LiH in Li batteries and resolve the debate between the proposed modes of LiH. Insight into the formation mechanism of LiH, its chemical origin, and performance consequences for Li batteries are also discussed.

RESULTS AND DISCUSSION

To study the existence of LiH in Li batteries, we cycle Li batteries prepared with mesh electrodes directly compatible with transmission electron microscope (TEM) sample holders. The charged anodes are plunge-frozen into liquid nitrogen in an inert atmosphere and transferred into the TEM. As in our recent development of cryogenic TEM for battery materials, cryogenic transfer of charged anodes enables their characterization while preventing side reactions with air during insertion into the microscope (*14*);

[1]Department of Materials Science and Engineering, Stanford University, Stanford, CA, USA. [2]Department of Chemistry, Stanford University, Stanford, CA, USA. [3]Department of Chemical Engineering, Stanford University, Stanford, CA, USA. [4]SLAC National Accelerator Laboratory, Stanford Institute for Materials and Energy Sciences, Menlo Park, CA, USA.
*Corresponding author. Email: yicui@stanford.edu

in addition, this simple preparation prevents ion beam–induced damage that can result from focused ion beam (FIB) milling (*15*, *16*). Cryo–scanning TEM (STEM) EELS mapping has proven a valuable technique to study air-sensitive battery materials with high spatial and chemical resolution (*7*, *17*–*19*). During cryo-STEM EELS of the charged Li anode in Fig. 1 (A and B), we spectroscopically confirm that both Li metal and LiH are present. The loss spectrum of Li metal is characterized by the surface plasmon maximum at 3.3 eV, volume plasmon maximum at 7.5 eV, and Li K-edge with an onset energy of 55 eV. The loss spectrum of LiH is characterized by the H K-edge maximum at 12.8 eV, volume plasmon maximum at 15.3 eV, and the Li K-edge onset at 57.5 eV. The shape of the Li K-edge core loss can be used for chemical identification; our measured spectra for Li metal and LiH in Fig. 1B closely match predicted absorption spectra (*20*, *21*) and previously measured standards (*7*). Additional measured examples of Li metal and LiH occurring within the same filament can be found in fig. S1.

Bulk LiH is an electrical insulator (*11*); however, the electronic properties of LiH formed in Li batteries have not been measured. Under appropriate conditions, the vibrational modes, electronic properties, and optical properties of materials can be studied in electron microscopes. Using a monochromated electron beam during cryo-STEM EELS, in Fig. 1C, we show the excitation of valence band electrons into the conduction band of LiH on a charged Li anode. Using the linear-fit method described elsewhere (*22*), we consistently measure a bandgap energy of 4.9 eV, clear spectroscopic evidence that LiH formed in Li batteries is a wide-bandgap electrical insulator. This experimental value is in good agreement with the predicted bandgap energy of 5.08 eV (*23*).

Cryo-STEM EELS mapping of loss features belonging to Li metal (red) and LiH (blue) in Fig. 1D reveals the coexistence of the two phases on the anode after charging. We find that LiH and Li metal typically occur within the same filament, forming sharp interfaces between the two phases, whereas Zachman *et al.* (*7*) proposed that LiH and Li metal electrodeposit into distinct morphologies. These contrasting results likely stem from the low-throughput sample preparation process used in their study. Zachman *et al.* used cryo-FIB milling to extract cross sections of individual Li dendrites, followed by transfer into the TEM, a low-throughput technique that limits the number of observations and can damage the highly reactive and beam sensitive sample. In our work, a mesh electrode that is directly compatible with TEM characterization increases the number of observations that we can make, resulting in improved confidence for our conclusion. Our observation that Li metal and LiH coexist within individual dendrites, in combination with our measurements of the electrically insulating properties of LiH, provides direct evidence that the electrical conduction pathway from the current collector to Li metal can be blocked by LiH.

Capacity loss mechanisms for Li metal anodes are driven by (i) formation of electrically isolated "dead" Li and (ii) side reactions of Li metal with electrolyte (including the reactions that form the SEI layer). Electrical isolation of Li metal from the current collector is proposed as the leading cause of capacity loss in Li metal batteries in many liquid electrolytes (*10*); however, this phenomenon remains poorly understood. The main theory currently explaining the formation of electrically isolated Li is the nonuniform dissolution of Li during battery discharge (*24*, *25*). Our results suggest the

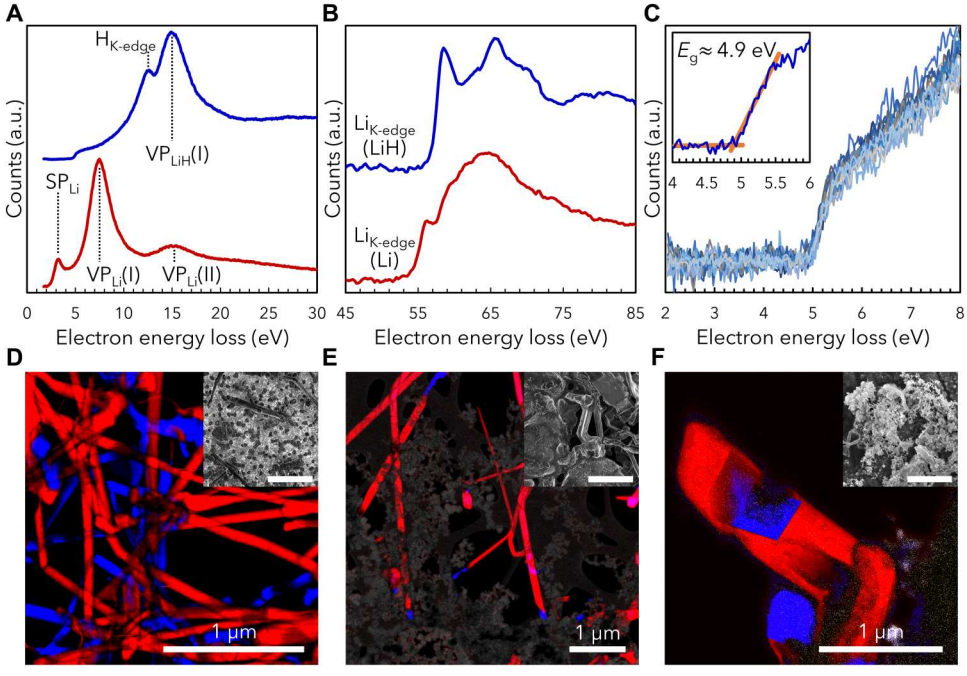

Fig. 1. Cryo-STEM EELS evidence of LiH and Li metal coexistence in Li batteries. (**A**) Monochromated low-loss EELS showing the H K-edge and volume plasmon of LiH and the surface plasmon and volume plasmons of Li metal. a.u., arbitrary units. (**B**) Li K-edge of Li metal and LiH phases. K-edge onset occurs at 55 and 57.5 eV in Li metal and LiH, respectively. (**C**) Valence band excitations of LiH measured with monochromated EELS. The inset demonstrates the linear-fit method used to calculate a bandgap energy of 4.9 eV. Cryo-STEM EELS mapping of features corresponding to Li metal (red) and LiH (blue) on (**D**) Li metal anodes and fast-charged (**E**) graphitic carbon anodes and (**F**) silicon anodes. The inset on cryo-STEM EELS maps are SEM images showing the morphology of the respective anode after charging. Scale bars, 5 μm.

discovery of a capacity loss mechanism in Li batteries, whereby Li metal can be electrically isolated by the insulating LiH phase.

While the performance of Li metal anodes has improved in recent years, Li-ion anodes remain the most widely adopted chemistry for Li batteries. Li-ion anodes store Li between van der Waals gaps (in the case of graphitic carbon) or by alloying with the host material (in the case of silicon). During fast charging of Li-ion anodes, Li dendrites can deposit on conductive surfaces of the anode (*26*, *27*). Li dendrites deposited during fast charging can penetrate the porous battery separator and cause catastrophic failure in Li-ion batteries (*28*). If Li metal can deposit on the surface of Li-ion anodes during fast charging, we propose that it is possible that LiH can form as well. To study this question, we perform cryo-STEM EELS characterization on both graphitic carbon and silicon anodes. By mapping spectral features belonging to Li metal and LiH with cryo-STEM EELS, we find that both Li metal and LiH exist on graphitic carbon (Fig. 1E) and silicon (Fig. 1F) anodes after fast charging. In the case of graphitic carbon anodes, we observe that LiH frequently interfaces between graphitic carbon and Li metal, electrically isolating Li metal from the graphitic carbon and the current collector. We believe that this finding helps explain capacity losses and buildup of electrically isolated dead Li after fast charging of Li-ion batteries (*29*, *30*).

Comparing our results to previous reports of LiH in Li batteries, two important observations from our cryo-STEM EELS maps can be made. Regarding the proposed SEI mode of LiH (*6*): If LiH is a chemical component of the SEI, we would expect to measure it at the surface of Li metal. However, we find no spectroscopic evidence of LiH in the SEI on Li metal. We believe that this result makes sense because any LiH in the SEI layer will react with the electrolyte given the permeability of the SEI (*31*) and the strong reductive nature of LiH (*11*). Regarding the proposed dendrite mode of LiH (*7*): We would expect to observe distinct dendrites of Li metal and LiH. However, in nearly all cases, we find that LiH interfaces directly with Li metal. The boundary between LiH and Li metal is defined by sharp interfaces, which, if well aligned, approaches the size of our STEM probe. We believe that this result indicates a conversion reaction between deposited Li metal dendrites and hydrogen rather than direct electrodeposition of LiH dendrites.

Our results add to the growing body of literature that supports the existence of LiH in Li batteries; however, the formation mechanism of LiH in Li batteries remains an open question. Our cryo-STEM EELS results suggest that hydrogen reacts with deposited Li metal to nucleate and grow LiH within Li metal dendrites rather than direct electrodeposition of LiH. Sharp boundaries between Li metal and LiH further suggest a crystallographic relationship between the body-centered cubic (BCC) structure of Li metal and the face-centered cubic (FCC) structure of LiH during the conversion reaction. To study this relationship in more detail, we use low-dose cryo–high-resolution TEM (HRTEM), which can provide crystallographic information with high spatial resolution while minimizing beam damage to the specimen (*32*). Figure 2A shows the low-dose cryo-HRTEM image at the Li metal–LiH boundary, and the corresponding selected area fast Fourier transforms (FFTs) are shown in Fig. 2 (B and C). The selected area FFTs show two distinct lattice spacings measured at 0.235 and 0.245 nm, belonging to LiH (1 1 1) and Li metal (1 1 0) respectively, which match our measured real space results (fig. S2). Analysis of the selected area FFT at the interface (fig. S3) shows the distinct lattice spacings and how this results in the observed Moiré pattern. This complements the cryo-STEM EELS result and provides crystallographic evidence that LiH exists within Li metal dendrites in Li batteries. Alternating dark and bright bands in the image across the Li metal–LiH boundary in Fig. 2A is a Moiré pattern resulting from the mismatch in interplanar spacing between LiH (1 1 1) and Li metal (1 1 0) and a slight misalignment of the interface relative to the optic axis in the TEM. The Fourier-filtered image of the spatial frequencies belonging to Li metal and LiH plotted in red and blue, respectively, in Fig. 2D shows a clear boundary between the two phases. Digitally zooming into the boundary and overlaying the crystal structures of Li metal and LiH, Fig. 2E shows the alternating close packed layers of Li and H along (1 1 1) planes of LiH are parallel (~0.7° mismatch) to the close packed (1 1 0) planes of Li metal. The difference in lattice parameter between the two phases introduce a coherency strain, resulting in a distortion of the metal phase at the Li metal–LiH interface (fig. S4).

The observed (1 1 0)//(1 1 1) orientation relationship between Li metal and LiH is similar to the well-known Nishiyama-Wasserman and Kurdjumov-Sachs type (1 1 1)//(1 1 0) orientation relationships during the austenite (FCC) → martensite (BCC) phase transformation in iron (*33*). This orientation relationship supports our hypothesis that LiH forms in Li batteries by a reaction of deposited Li metal with hydrogen, which induces the BCC → FCC phase transformation. The reaction of Li metal with hydrogen and the resulting phase transformation are schematically illustrated in Fig. 2F. Sharp interface termination measured during cryo-STEM EELS in combination with the (1 1 0)//(1 1 1) crystallographic relationship measured during low-dose cryo-HRTEM suggest a preferential interface structure, which is likely governed by the minimization of coherency strain at the Li metal–LiH phase boundary (*34*).

For the reaction of Li metal into LiH to proceed in Li batteries, hydrogen must diffuse through the SEI and toward Li metal. In this case, the composition and structure of the SEI likely play a role in the diffusivity. To explore this in more detail, we perform low-dose cryo-HRTEM on the SEI on Li metal and LiH (Fig. 3, A and B). An important observation is that LiH is not directly exposed to the electrolyte. Instead, we find that LiH has its own passivating SEI layer, likely explaining why LiH formed in Li batteries is not completely consumed by reactions with the electrolyte. Compared to the SEI on Li metal (≈20 nm), the SEI on LiH thickness varies between 25 and 40 nm with well-defined crystalline grains. FFTs of the low-dose cryo-HRTEM images of the SEI on Li metal and LiH are shown in Fig. 3 (C and D). FFT analysis of the SEI on Li metal shows a diffuse ring near the spatial frequency of Li_2O (1 1 1) planes, suggesting that the SEI on Li metal is predominantly amorphous with nanocrystalline Li_2O grains and organic Li alkyl carbonates (*35*, *36*). An additional example of the SEI on Li metal and the diffuse Li_2O (1 1 1) reflection is shown in fig. S5. A similar analysis on LiH reveals a different result: The SEI interfacing LiH is rich in crystalline grains of LiOH, as demonstrated by strong reflections measured at the spatial frequency of (0 0 1) planes of LiOH. Differences between the SEIs are shown more clearly in the Fourier-filtered images by plotting the spatial frequencies corresponding to Li metal, LiH, and LiOH phases in red, blue, and yellow, respectively, in Fig. 3 (E and F). In these images, crystalline grains of LiOH are clearly resolved in the SEI on LiH, whereas no large crystalline grains are resolved in the SEI on Li metal. The reaction of H_2O impurities with Li metal and LiH would both evolve hydrogen gas and form LiOH;

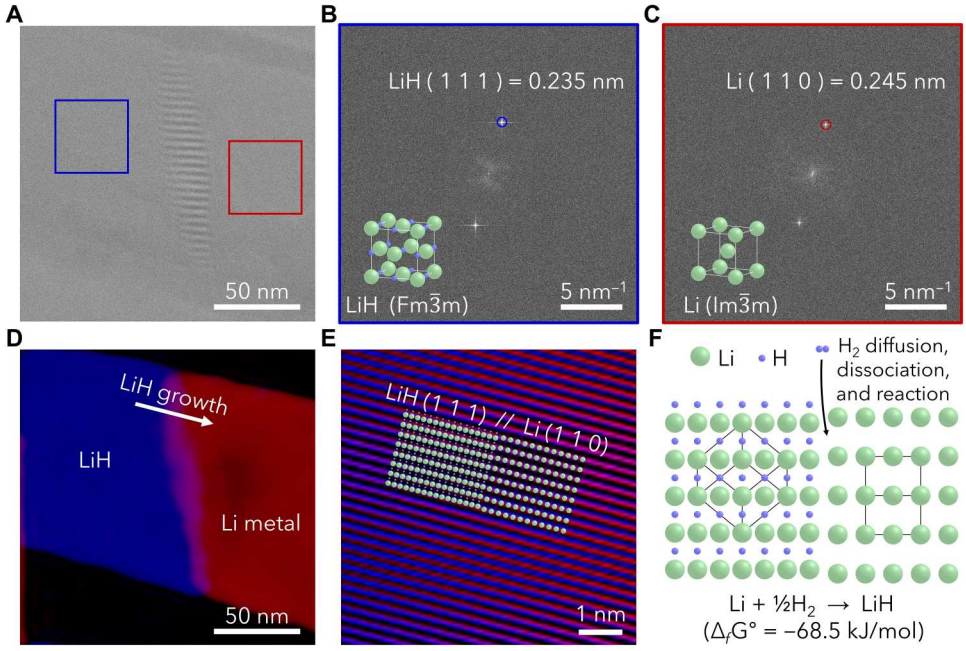

Fig. 2. Crystallographic orientation relationship at the Li metal-LiH boundary. (**A**) Low-dose cryo-HRTEM image of a single Li dendrite. Alternating light and dark bands across the Li dendrite is a Moiré pattern resulting from the lattice spacing mismatch and slight misalignment of the interface relative to the optic axis of the TEM. (**B**) Selected area FFT from the region highlighted in blue (to the left of the Moiré pattern). The measured spacing matches the (1 1 1) interplanar spacing of LiH. (**C**) Selected area FFT from the region highlighted in red (to the right of the Moiré pattern). This spacing matches the (1 1 0) interplanar spacing of Li metal. (**D**) Fourier-filtered image with spatial frequencies corresponding to Li metal and LiH are plotted in red and blue, respectively. (**E**) Digitally zoomed image of the LiH-Li metal interface. (1 1 1) planes of LiH are aligned to the (1 1 0) planes of Li metal. (**F**) Schematic of the proposed reaction mechanism where hydrogen diffuses, dissociates into atomic hydrogen, and reacts with Li metal to nucleate and grow LiH.

in this case, the evolved hydrogen could further react with Li metal to form LiH, likely explaining the frequent observation of LiOH in the SEI near LiH. Contrary to the SEI mode of LiH proposed by Shadike *et al.* (*6*), we find no crystallographic evidence of LiH in the tens of nanometers thick SEI, further confirming our cryo-STEM EELS result that LiH is not present in the SEI. While the lithium salt and carbonate solvents used in the work by Shadike *et al.* (*6*) are different from those in our study, our results suggest that LiH and Li metal measured in the residual layer likely arise from isolation and buildup of both species. Our study highlights the importance of combining multiscale approaches to identify species in the nanometer-scale interphase between lithium metal and the electrolyte.

In Li batteries, hydrogen evolution occurs when (i) H_2O impurities are reduced and (ii) during cathode-anode cross-talk (from solvent oxidation, migration, and reduction) (*5*). LiH has a negative standard Gibbs free energy of formation, meaning that it is energetically favorable to form from Li metal and hydrogen. The morphology of electrodeposited Li metal in LP40 electrolyte is predominantly filamentary (high surface area compared to a bulk film), suggesting that accumulated hydrogen gas can react to form LiH, even at room temperature. To study the formation of LiH from evolved hydrogen during cycling, we control hydrogen evolution by (i) controlling the amount of H_2O impurities in the electrolyte and (ii) using Li-Cu half-cells (to prevent hydrogen evolution from cathode-anode cross-talk). It is important to note that in full cell Li batteries, hydrogen evolution will occur from both water impurities and cathode-anode cross-talk. Figure 4A shows the ^1H nuclear magnetic resonance (NMR) spectrum of dilute water impurities [~100–parts per million (ppm) H_2O] in ethylene carbonate: diethyl carbonate:1 M $LiPF_6$ (LP40), a standard electrolyte for Li metal and Li-ion batteries, compared to the spectrum of dried LP40 electrolyte where this characteristic peak is minimized. Hydrogen evolution from the reduction of H_2O in carbonate electrolytes has an onset potential of 2 V versus Li/Li^+ (*37*). By performing linear sweep voltammetry (LSV) with a three-electrode cell, we show that hydrogen evolution is minimized by thoroughly drying the electrolyte (Fig. 4B). After confirming minimization of H_2O impurities and hydrogen evolution in the dried electrolyte, in Fig. 4C, we compare the half-cell cycling efficiency using the control and dried LP40 electrolytes. During cycling, the half-cell efficiency in the control LP40 electrolyte quickly decays below 85% and reaches a minimum of 70% after 50 cycles. In comparison, using the dried LP40 electrolyte, the half-cell cycling efficiency stabilizes above 90% efficiency and maintains this efficiency for more than 50 cycles, a marked improvement over the control LP40 electrolyte. A detailed comparison of the nucleation overpotential, cycling overpotential, and Coulombic efficiency for multiple cells using both control LP40 and dried LP40 are shown in fig. S6.

Improved cycling efficiency after drying demonstrates that preventing hydrogen evolution is an effective strategy to improve Li metal anode reversibility. To understand whether H_2O impurities are responsible for LiH formation at the electrode scale, in Fig. 4D, we compare XRD patterns of Li metal anodes charged in the control and dried LP40 electrolytes. In the control LP40 electrolyte, peaks corresponding to Li metal (1 1 0) and LiH (1 1 1) are both

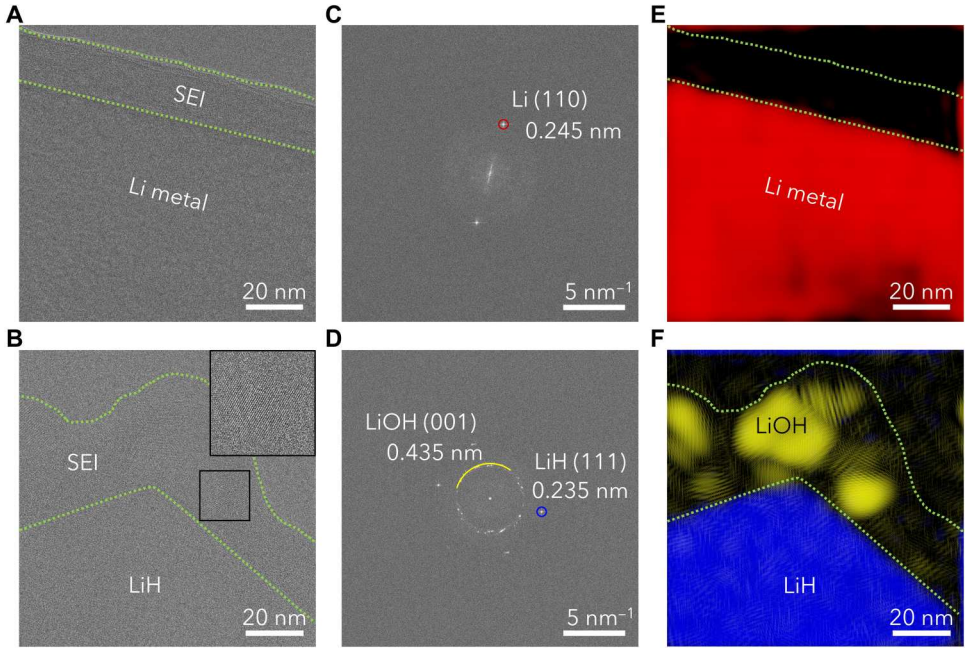

Fig. 3. Cryo-HRTEM comparison of the SEI on Li metal and LiH. Low-dose cryo-HRTEM image of the SEI (outlined in green) on (**A**) Li metal and (**B**) LiH. (**C**) FFT of the image in (A) reveals that the SEI on the crystalline Li metal lattice is uniformly amorphous/nanocrystalline. (**D**) FFT of the image in (B) reveals that the SEI on LiH consists of polycrystalline LiOH with no obvious texturing to the LiH lattice. Fourier-filtered images of (**E**) the SEI on Li metal and (**F**) the SEI on LiH with the spatial frequencies of corresponding to Li metal (1 1 0), LiH (1 1 1), and LiOH (0 0 1) plotted in red, blue, and yellow, respectively.

observed. To verify that this peak belongs to LiH and not LiF (given the nearly identical lattice spacings) (*6*), we expose the charged anode to atmosphere. In this case, Li metal and LiH both react with moisture in the air to form LiOH, in contrast to LiF, which is stable in air. After 1 hour of air exposure, we find that the peaks related to Li metal and LiH disappear and those of LiOH appear, verifying the presence of LiH on the charged anode and confirming the coexistence of LiH and Li metal in Li batteries measured during our cryo-HRTEM and cryo-STEM EELS measurements. In the case of the dried electrolyte, we are not able to resolve the (1 1 1) peak of LiH; this demonstrates that controlling H_2O impurities, which evolve hydrogen when reduced, is an effective strategy to minimize LiH formation and improve Li battery cycling efficiency. Similarly, when we perform cryo-STEM EELS of electrodeposited Li using the dried LP40 electrolyte, we observe less LiH (fig. S7).

Our results link hydrogen evolution in Li batteries to LiH formation, whereby even dilute H_2O impurities in common commercial Li electrolytes can markedly decrease battery reversibility and cause capacity losses. We propose that evolved hydrogen in Li batteries can cause capacity losses through (i) the chemical reaction between hydrogen and Li metal to form LiH (Fig. 4E) and (ii) electrical isolation of Li metal by insulating LiH (Fig. 4F). Evidence of the electrical isolation of Li metal from the current collector by LiH is shown in fig. S8, supporting our proposed mechanism. Given the low concentration of H_2O impurities in the control LP40 electrolyte, the magnitude of efficiency improvements after drying the electrolyte, and the electrically insulating nature of LiH, we conclude that electrical isolation of Li metal by LiH is the primary capacity loss mechanism resulting from hydrogen evolution in Li batteries.

Considering that bulk synthesis of LiH requires high temperatures and hydrogen pressures to proceed at appreciable rates (*9*), it is interesting to consider how LiH forms in Li batteries. Near–room temperature synthesis of LiH has been reported; however, the sluggish kinetics limits the reaction to the surface (*38*). One important distinction here is that the morphology of electrodeposited Li metal is far from bulk. In this case, Li typically deposits as long filamentary dendrites with diameters ranging from tens to hundreds of nanometers. This nanoscale morphology likely facilitates the formation of LiH in Li batteries by a high surface area to volume ratio, increased sites for hydrogen absorption, and minimization of coherency strain at the Li metal–LiH phase boundary (by minimizing the interface area). It is clear from our results that LiH formation is detrimental to Li battery reversibility and can cause capacity losses, likely originating from the electrical isolation of dead Li metal. We believe that preventing water contamination, controlling Li morphology, and electrolyte formulations that decrease hydrogen evolution will prove useful strategies to improve the performance of Li batteries by minimizing LiH formation.

MATERIALS AND METHODS

Coin-cell preparation

Type-2032 coin cells were prepared in an argon glove box (<0.2-ppm O_2 and <0.01-ppm H_2O). High-purity lithium metal [750 μm, 99.9% (Alfa Aesar)] counter electrodes are prepared by cleaning the surface with a polyethylene scraper to remove the surface layer until the foil has a metallic luster and then cut into a 1-cm^2 disk. A single stainless-steel (SS) ring spring is placed on the anode cap, followed by a single SS spacer on which the lithium metal is placed. Twenty microliters of electrolyte is placed directly onto the

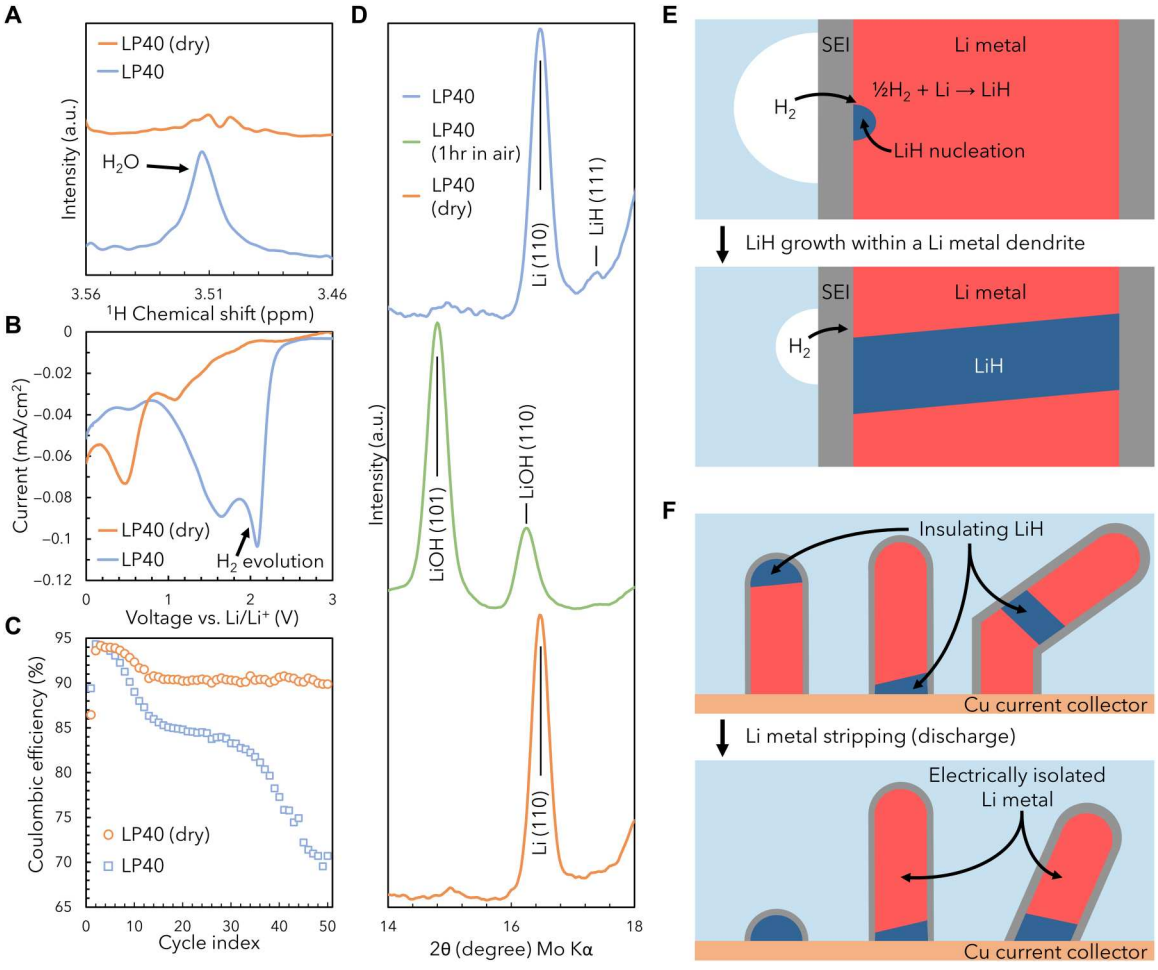

Fig. 4. Relationship between H_2O impurities, hydrogen evolution, LiH formation, and cycling performance in Li batteries. (**A**) ^1H NMR spectrum of trace water impurities in LP40 electrolyte compared to dried LP40 electrolyte. The water peak at 3.51 ppm is minimized after drying. (**B**) Three-electrode (copper working electrode, Li metal counter, and reference electrodes) LSV curve demonstrating that drying the electrolyte effectively minimizes H_2O reduction and, thereby, hydrogen evolution. (**C**) Li-Cu half-cell cycling performance showing that minimizing H_2O impurities and hydrogen evolution can markedly improve anode reversibility. (**D**) XRD pattern of hermetically sealed charged metal anodes in LP40 electrolyte, LP40 electrolyte (after 1 hour of air exposure), and dried LP40 electrolyte. Air exposure of the charged anode in LP40 electrolyte demonstrates that the spacing near 0.23 nm belongs to LiH (1 1 1) and not to the air stable LiF (1 1 1). XRD pattern of the charged anode in dried LP40 electrolyte demonstrates that limiting hydrogen evolution minimizes LiH formation. (**E**) Schematic of the reaction between hydrogen and a Li metal dendrite. In this case, hydrogen diffuses through the SEI, dissociates, and reacts with Li metal. This reaction nucleates the insulating LiH phase within Li metal dendrites and continues to grow until hydrogen is depleted. (**F**) Schematic of the formation of electrically isolated Li metal during discharge for Li dendrites poisoned with LiH. Electrically insulating LiH breaks the electrical conduction path between the Cu current collector and Li metal.

lithium metal electrode, followed by a single layer of polymer separator (25 μm of polypropylene/polyethylene/polypropylene; Celgard); another 20 μl of electrolyte is then placed directly on the top surface of the separator (for a total volume of electrolyte is 40 μl). The working electrode is then placed directly on the separator, followed by a single SS spacer, and, lastly, the cathode cap. Working electrodes used here are either copper foil (Pred Materials), graphite electrodes on copper foil, silicon electrodes coated on copper foil, or copper TEM grids (Ted Pella) loaded with the working material and placed on top of the respective electrode. Coin cells are then crimped and sealed with a polymer O-ring to create an airtight seal and transferred out of the glove box.

Coin-cell electrochemistry

All electrochemical experiments on coin cells were done using a 96-channel Arbin battery testing system. Metal anodes to be used for TEM and scanning electron microscopy (SEM) experiments charged with a current density of 1 mA cm^{-2} up to a capacity of 0.2 mA hour cm^{-2}. Lithium-ion anodes used in TEM experiments were charged with a C-rate of 3C until the nominal capacity of the backing electrode was reached. Lithium metal half-cell cycling measurements were performed by charging at 1 mA cm^{-2} up to a capacity of 1 mA hours cm^{-2} and discharged at 1 mA cm^{-2} until the cutoff voltage of 1 V (versus Li/Li^+) was reached. Coulombic efficiency was calculated by normalizing the discharged capacity by the charging capacity and reported as a percentage. Coulombic efficiency measurements were performed and averaged over three cells with both electrolytes.

Air-free cryogenic sample transfer

Coin cells containing charged TEM grids were transferred into an argon glove box. The coin cells were then disassembled, and the charged TEM grid is extracted and placed onto a clean Kimwipe. To remove and prevent dissolved salts from crystallizing on TEM grids, 10 μl of dimethyl carbonate (dried using molecular sieves) is directly dropped onto the TEM grid, which was quickly absorbed by the Kimwipe. The TEM grid is then placed into a primary crushable air-tight vessel, which is placed into a larger secondary silicone sealed container and transferred out of the glove box. Five millibars of argon overpressure was maintained when sealing both vessels to minimize any contamination during the 3-s walk from the glove box antechamber to the plunge-freezing station. The secondary container is then opened, and the primary container is quickly plunged into a 50-mm-deep bath of liquid nitrogen and crushed after 2 s in the bath. This directly plunges the TEM grid into the liquid nitrogen under an argon atmosphere, preventing the charged anode from reacting with the CO_2, O_2, N_2, and H_2O in the air. While submerged in liquid nitrogen, the TEM grid is placed into a cryogenic grid storage box. The cryogenic storage box containing the frozen TEM grid is placed in a glass scintillator vial (filled with liquid nitrogen) and transferred into a 3-liter Dewar filled with liquid nitrogen and taken to the TEM room. While submerged in liquid nitrogen, the TEM grid was loaded into a cryo-TEM holder (Gatan 626) in a cryo-transfer station and inserted into the column of the TEM. The cryo-TEM holder uses a shutter to hold a small volume of liquid nitrogen, which minimizes the likelihood of air exposure and water condensation onto the sample during the brief removal from the cryo-transfer station and evacuation in the column down below 10^{-6} torr, preserving the specimen in its native state. Throughout the transfer process and during the experiment, the sample temperature was maintained at or below −176°C.

Cryo-STEM EELS measurement

Cryo-STEM EELS measurements are carried out using an FEI Titan 80-300 environmental (scanning) TEM operated with accelerating voltage of 80 kV for monochromated EELS and 300 kV for standard EELS. Samples are prepared and loaded as described in the coin-cell preparation, coin-cell electrochemistry, and air-free cryogenic sample transfer methods. The beam current was maintained between 50 and 100 pA; the pixel dwell time was maintained between 1 and 1.5 ms, and a camera length of 130 mm was used for all EELS measurements. EELS spectra were acquired on a GIF Quantum 966 with a dispersion of 0.025 eV for monochromated EELS and 0.25 eV for standard EELS. The full width at half maximum of the zero-loss peak during standard EELS was measured to be 1.5 eV and between 0.125 and 0.200 eV during monochromated EELS. Pixel-by-pixel energy correction during EELS spectrum imaging was corrected by centering the zero-loss peak to 0 eV, correcting for both instrument-induced oscillations and monochromator drift. To ensure precise energy correction, the zero-loss peak and EELS spectra are collected simultaneously with the same dwell time (this limits the dwell time on the detector but provides the most accurate energy correction). After energy correction, the low-loss spectrums and Li-K edge core loss spectrums of lithium metal and LiH were binned over a 25-nm^2 area and then background subtracted by fitting a power law before the features of interest. EELS spectrum images were generated by subtracting the background and plotting the intensity of the lithium metal and LiH volume plasmon (2-eV energy window centered at the maximum of the volume plasmon energy). Bandgap measurement of LiH were performed by a similar procedure of energy drift correction, binning, and background subtraction. Spectrums for bandgap measurement of LiH were binned over a 25-nm^2 region on 15 unique samples of LiH away from the lithium metal/LiH and LiH/SEI interface. A linear fit of the background (between 2 and 4.5 eV) and the initial linear region of the valence band excitation (between 5 and 5.4 eV) is performed, and the bandgap is measured by calculating the intercept of these two fits.

Low-dose cryo-HRTEM measurement

Low-dose cryo-HRTEM measurements are carried out using an FEI Titan 80-300 environmental (scanning) TEM operated with accelerating voltage of 300 kV equipped with a Gatan K3 IS direct electron detector operated in counting mode with dose fractionization. Before sample insertion, the condenser lens apertures, condenser lens astigmatism, beam tilt pivot points, and the rotation center are aligned and corrected. Following basic alignments, third-order axial aberrations (twofold axial astigmatism, second-order axial coma, threefold axial astigmatism, third-order spherical aberration, fourfold axial astigmatism, and axial star aberration) are corrected and minimized using the Zemlin-tableau method. Samples are prepared and loaded as described in the coin-cell preparation, coin-cell electrochemistry, and air-free cryogenic sample transfer methods. At low magnification (electron dose < 0.5 e^- $Å^{-2}$ s^{-1}), a sample is identified and aligned by tilting until the (1 1 0) plane of lithium metal is strongly diffracting (as observed with selected area diffraction) as to meet the two-beam condition. The sample is then focused to minimum contrast using the stage control, and a large negative defocus is added using the objective lens to provide contrast during focusing. Away from the area of interest, a region at a similar height is identified and is used to find the optimal defocus for imaging (ensuring that sample illumination is away from the area of interest). Using low-dose acquisition mode, the beam is shifted, proper defocus is set, and condenser and projector lens currents are set, while the electron beam is behind a shutter and illumination occurs only during image acquisition, minimizing total dose to ~75 e^- $Å^{-2}$ at a dose rate of 75 e^- $Å^{-2}$ s^{-1}. Lattice spacings were measured using a selected area FFT over the area of interest; the distance from the center of the FFT to the center of mass of the bright spots is measured, and the inverse of the spatial frequency is the interplanar spacing. Interplanar spacings are compared to theoretical and experimental values of the crystal structure and used in combination with the spectroscopy methods described in the EELS methods to identify the phase of lithium. Fourier-filtered images were computed by identifying the relevant crystallographic phases of lithium in the image, masking the FFT to segregate phases (by spatial frequency), inversing the FFT, and lastly summing the images color-coded corresponding to the phase of lithium.

Three-electrode measurement

LSV was performed with three-electrode beaker cells in an argon-filled glove box. Cu wire with a 0.005-cm^2 area was embedded into an insulating and chemically resistant epoxy and used as the working electrode. Lithium foils were used as both the reference and counter electrodes, so the potential is versus the Li/Li^+ equilibrium potential. Before each LSV experiment, the Cu electrode was

polished with a 2000-grit sandpaper. The open circuit potential was typically around 2 V, and the Cu electrode was then scanned linearly to 0 V with a scan rate of 10 mV/s.

NMR measurement

^{1}H NMR was performed on a Varian Mercury 400 MHz NMR. The temperature was set at 25°C. Samples were prepared in the glove box by injecting 300 μl of electrolyte into a new and dried NMR tube, together with 600 μl of methyl sulfoxide-d6 (Acros Organics, 99.9% D, maximum 0.03% water impurity). It was then sealed with polytetrafluoroethylene caps and immediately put into the NMR machine for data acquisition. The samples were locked and shimmed using the external standard.

XRD measurement

Lithium deposited onto copper electrodes were disassembled and extracted from coin cells in an argon glove box (<0.2-ppm O_2 and <0.01-ppm H_2O), rinsed with a small volume of dimethyl carbonate (dried with molecular sieves), hermetically sealed in a primary polyester/polyethylene laminated Kapak pouch bag (thickness, ~65 μm), and further sealed in a secondary container with a silicone seal (sealing was performed with 5 mbar of argon overpressure to minimize air exposure). XRD patterns were recorded on a Bruker D8 Discovery x-ray diffractometer with Mo Kα radiation source (λ = 0.7107 Å) in transmission mode. The exposure time was set to 300 s, and the resulting ring pattern was radially integrated to produce the 2θ plot. The interplanar spacing was calculated according to Bragg's law [$n\lambda = 2d\sin(\theta)$], where λ is the wavelength of the x-ray source, n is a positive integer, d is the interplanar distance, and θ is the peak angle measured from the XRD pattern. Confirmation of LiH (to the crystallographically similar LiF) was performed by exposing the sealed electrode to air and monitoring the evolution of the LiH peak. Given that LiH will react with humidity in atmosphere to produce LiOH and LiF is stable at similar time scales, peak disappearance confirms that this peak belongs to LiH and not LiF. Air exposure was performed by cutting the sealed bag open, while the sample is mounted and the measurement is repeated (after 1 hour of air exposure).

Scanning electron microscopy

Lithium deposited onto copper electrodes were disassembled and extracted from coin cells in an argon glove box (<0.2-ppm O_2 and <0.1-ppm H_2O), rinsed with a small volume of dimethyl carbonate (dried with molecular sieves), mounted onto an SEM stage, and sealed in a secondary container with a silicone seal (sealing was performed with 5 mbar of argon overpressure to minimize air exposure). The sample was the loaded into the SEM (FEI Magellan 400 XHR) and pumped to the nominal pressure. Imaging was performed with a 1-kV accelerating voltage, 4-mm working distance, 90-pA beam current, and a +500-V stage bias.

Materials preparation

3A molecular sieves (eight mesh) were cleaned and dried, transferred into an argon glove box (<0.2-ppm O_2 and <0.01-ppm H_2O), regenerated in an oven at 250°C for 12 hours, and allowed to slowly cool back to room temperature. A 1:1 (v/v) mixture of ethylene carbonate (99+%; Acros) and diethyl carbonate (>99% anhydrous; Sigma-Aldrich) was prepared in the glove box and then dried over 4A molecular sieves for at least 1 week to achieve minimal H_2O impurities. In the glove box, $LiPF_6$ salt (≥99.99% trace metals basis; Sigma-Aldrich) was dried at 65°C for 48 hours to minimize any H_2O impurities in the salt. The dried electrolyte was then prepared by mixing the salt with the 1:1 (v/v) mixture of ethylene carbonate and diethyl carbonate to achieve a 1 M concentration. All coin-cell materials were then dried in the glove box oven at 50°C for 2 hours before cell assembly.

Supplementary Materials

This PDF file includes:

Figs. S1 to S8

REFERENCES AND NOTES

1. J. Vetter, P. Novák, M. R. Wagner, C. Veit, K. C. Möller, J. O. Besenhard, M. Winter, M. Wohlfahrt-Mehrens, C. Vogler, A. Hammouche, Ageing mechanisms in lithium-ion batteries. *J. Power Sources* **147**, 269–281 (2005).
2. D. Aurbach, E. Zinigrad, Y. Cohen, H. Teller, A short review of failure mechanisms of lithium metal and lithiated graphite anodes in liquid electrolyte solutions. *Solid State Ion.* **148**, 405–416 (2002).
3. D. P. Finegan, E. Darcy, M. Keyser, B. Tjaden, T. M. M. Heenan, R. Jervis, J. J. Bailey, N. T. Vo, O. V. Magdysyuk, M. Drakopoulos, M. Di Michiel, A. Rack, G. Hinds, D. J. L. Brett, P. R. Shearing, Identifying the cause of rupture of Li-ion batteries during thermal runaway. *Adv. Sci.* **5**, 1700369 (2018).
4. Q. Wang, P. Ping, X. Zhao, G. Chu, J. Sun, C. Chen, Thermal runaway caused fire and explosion of lithium ion battery. *J. Power Sources* **208**, 210–224 (2012).
5. M. Metzger, B. Strehle, S. Solchenbach, H. A. Gasteiger, Origin of H_2 evolution in LIBs: H_2O reduction vs. electrolyte oxidation. *J. Electrochem. Soc.* **163**, A798 (2016).
6. Z. Shadike, H. Lee, O. Borodin, X. Cao, X. Fan, X. Wang, R. Lin, S.-M. Bak, S. Ghose, K. Xu, C. Wang, J. Liu, J. Xiao, X.-Q. Yang, E. Hu, Identification of LiH and nanocrystalline LiF in the solid–electrolyte interphase of lithium metal anodes. *Nat. Nanotechnol.* **16**, 549–554 (2021).
7. M. J. Zachman, Z. Tu, S. Choudhury, L. A. Archer, L. F. Kourkoutis, Cryo-STEM mapping of solid–liquid interfaces and dendrites in lithium-metal batteries. *Nature* **560**, 345–349 (2018).
8. D. Aurbach, I. Weissman, On the possibility of LiH formation on Li surfaces in wet electrolyte solutions. *Electrochem. Commun.* **1**, 324–331 (1999).
9. K. Moers, Untersuchungen über den Salzcharakter des Lithiumhydrids. *Zeitschrift für Anorg. und Allg. Chemie* **113**, 179–228 (1920).
10. C. Fang, J. Li, M. Zhang, Y. Zhang, F. Yang, J. Z. Lee, M.-H. Lee, J. Alvarado, M. A. Schroeder, Y. Yang, B. Lu, N. Williams, M. Ceja, L. Yang, M. Cai, J. Gu, K. Xu, X. Wang, Y. S. Meng, Quantifying inactive lithium in lithium metal batteries. *Nature* **572**, 511–515 (2019).
11. R. L. Smith, J. W. Miser, J. W. Miser, Compilation of the properties of lithium hydride (NASA, 1963).
12. G. Xu, J. Li, C. Wang, X. Du, D. Lu, B. Xie, X. Wang, C. Lu, H. Liu, S. Dong, G. Cui, L. Chen, The formation/decomposition equilibrium of LiH and its contribution on anode failure in practical lithium metal batteries. *Angew. Chemie* **133**, 7849–7855 (2021).
13. Y. Xiang, M. Tao, G. Zhong, Z. Liang, G. Zheng, X. Huang, X. Liu, Y. Jin, N. Xu, M. Armand, J.-G. Zhang, K. Xu, R. Fu, Y. Yang, Quantitatively analyzing the failure processes of rechargeable Li metal batteries. *Sci. Adv.* **7**, eabj3423 (2021).
14. Y. Li, Y. Li, A. Pei, K. Yan, Y. Sun, C. L. Wu, L. M. Joubert, R. Chin, A. L. Koh, Y. Yu, J. Perrino, B. Butz, S. Chu, Y. Cui, Atomic structure of sensitive battery materials and interfaces revealed by cryo–electron microscopy. *Science* **358**, 506–510 (2017).
15. J. Mayer, L. A. Giannuzzi, T. Kamino, J. Michael, TEM sample preparation and FIB-induced damage. *MRS Bull.* **32**, 400–407 (2011).
16. N. D. Bassim, B. T. De Gregorio, A. L. D. Kilcoyne, K. Scott, T. Chou, S. Wirick, G. Cody, R. M. Stroud, Minimizing damage during FIB sample preparation of soft materials. *J. Microsc.* **245**, 288–301 (2012).
17. Z. Zhang, Y. Cui, R. Vila, Y. Li, W. Zhang, W. Zhou, W. Chiu, Y. Cui, Cryogenic electron microscopy for energy materials. *Acc. Chem. Res.* **54**, 3505–3517 (2021).
18. D. T. Boyle, W. Huang, H. Wang, Y. Li, H. Chen, Z. Yu, W. Zhang, Z. Bao, Y. Cui, Corrosion of lithium metal anodes during calendar ageing and its microscopic origins. *Nat. Energy* **6**, 487–494 (2021).
19. W. Huang, H. Wang, D. T. Boyle, Y. Li, Y. Cui, Resolving nanoscopic and mesoscopic heterogeneity of fluorinated species in battery solid-electrolyte interphases by cryogenic electron microscopy. *ACS Energy Lett.* **5**, 1128–1135 (2020).

20. A. Jain, S. P. Ong, G. Hautier, W. Chen, W. D. Richards, S. Dacek, S. Cholia, D. Gunter, D. Skinner, G. Ceder, K. A. Persson, Commentary: The materials project: A materials genome approach to accelerating materials innovation. *APL Mater.* **1**, 011002 (2013).
21. K. Mathew, C. Zheng, D. Winston, C. Chen, A. Dozier, J. J. Rehr, S. P. Ong, K. A. Persson, Data descriptor: High-throughput computational x-ray absorption spectroscopy. *Sci. Data* **5**, 1–8 (2018).
22. J. Park, S. Heo, J. G. Chung, H. Kim, H. I. Lee, K. Kim, G. S. Park, Bandgap measurement of thin dielectric films using monochromated STEM-EELS. *Ultramicroscopy* **109**, 1183–1188 (2009).
23. D. J. Singh, Electronic structure calculations with the Tran-Blaha modified Becke-Johnson density functional. *Phys. Rev. B Condens. Matter Mater. Phys.* **82**, 205102 (2010).
24. Y. Li, W. Huang, Y. Li, A. Pei, D. T. Boyle, Y. Cui, Correlating structure and function of battery interphases at atomic resolution using cryoelectron microscopy. *Joule* **2**, 2167–2177 (2018).
25. R. A. Vilá, W. Huang, Y. Cui, Nickel impurities in the solid-electrolyte interphase of lithium-metal anodes revealed by cryogenic electron microscopy. *Cell Rep. Phys. Sci.* **1**, 100188 (2020).
26. K. G. Gallagher, S. E. Trask, C. Bauer, T. Woehrle, S. F. Lux, M. Tschech, P. Lamp, B. J. Polzin, S. Ha, B. Long, Q. Wu, W. Lu, D. W. Dees, A. N. Jansen, Optimizing areal capacities through understanding the limitations of lithium-ion electrodes. *J. Electrochem. Soc.* **163**, A138–A149 (2016).
27. P. Arora, M. Doyle, R. E. White, Mathematical modeling of the lithium deposition overcharge reaction in lithium-ion batteries using carbon-based negative electrodes. *J. Electrochem. Soc.* **146**, 3543–3553 (1999).
28. T. Waldmann, B. I. Hogg, M. Wohlfahrt-Mehrens, Li plating as unwanted side reaction in commercial Li-ion cells – A review. *J. Power Sources* **384**, 107–124 (2018).
29. K. Märker, C. Xu, C. P. Grey, Operando NMR of NMC811/graphite lithium-ion batteries: Structure, dynamics, and lithium metal deposition. *J. Am. Chem. Soc.* **142**, 17447–17456 (2020).
30. J. Wandt, P. Jakes, J. Granwehr, R. A. Eichel, H. A. Gasteiger, Quantitative and time-resolved detection of lithium plating on graphite anodes in lithium ion batteries. *Mater. Today* **21**, 231–240 (2018).
31. Z. Zhang, Y. Li, R. Xu, W. Zhou, Y. Li, S. T. Oyakhire, Y. Wu, J. Xu, H. Wang, Z. Yu, D. T. Boyle, W. Huang, Y. Ye, H. Chen, J. Wan, Z. Bao, W. Chiu, Y. Cui, Capturing the swelling of solid-electrolyte interphase in lithium metal batteries. *Science* **375**, 66–70 (2022).
32. Y. Li, K. Wang, W. Zhou, Y. Li, R. Vila, W. Huang, H. Wang, G. Chen, G. H. Wu, Y. Tsao, H. Wang, R. Sinclair, W. Chiu, Y. Cui, Cryo-EM structures of atomic surfaces and host-guest chemistry in metal-organic frameworks. *Matter* **1**, 428–438 (2019).
33. P. M. Kelly, A. Jostsons, R. G. Blake, The orientation relationship between lath martensite and austenite in low carbon, low alloy steels. *Acta Metall. Mater.* **38**, 1075–1081 (1990).
34. R. B. Schwarz, A. G. Khachaturyan, Thermodynamics of open two-phase systems with coherent interfaces: Application to metal-hydrogen systems. *Acta Mater.* **54**, 313–323 (2006).
35. D. Aurbach, Y. Ein-Ely, A. Zaban, The surface chemistry of lithium electrodes in alkyl carbonate solutions. *J. Electrochem. Soc.* **141**, L1–L3 (1994).
36. A. Schechter, D. Aurbach, H. Cohen, X-ray photoelectron spectroscopy study of surface films formed on Li electrodes freshly prepared in alkyl carbonate solutions. *Langmuir* **15**, 3334–3342 (1999).
37. D. Strmcnik, I. E. Castelli, J. G. Connell, D. Haering, M. Zorko, P. Martins, P. P. Lopes, B. Genorio, T. Østergaard, H. A. Gasteiger, F. Maglia, B. K. Antonopoulos, V. R. Stamenkovic, J. Rossmeisl, N. M. Markovic, Electrocatalytic transformation of HF impurity to H_2 and LiF in lithium-ion batteries. *Nat. Catal.* **1**, 255–262 (2018).
38. M. R. J. Perlow, W. C. Johnson, thesis, University of Chicago (1941).

Acknowledgments

Funding: The cryo-TEM research was supported by the Department of Energy, Office of Basic Energy Sciences, Division of Materials Science and Engineering under contract DE-AC02-76SF00515 (to Y.C. and J.A.D). R.A.V. acknowledges support from the National Academy of Sciences Ford Foundation Fellowship, the National Science Foundation Graduate Research Fellowship Program (NSF GRFP; grant no. DGE-1656518), and the Enhancing Diversity in Graduate Education (EDGE) Doctoral Fellowship Program at Stanford University. Part of this work was performed at the Stanford Nano Shared Facilities (SNSF), supported by the NSF under award ECCS-2026822. **Author contributions:** R.A.V. and Y.C. conceived the project and designed the experiments. R.A.V., W.Z., P.S., Y.Ye, and Y.Ya. prepared the electrolytes, electrodes, batteries, and TEM specimens used in this study. R.A.V., A.D., and W.Z. carried out cryo-STEM EELS measurements. R.A.V. performed low-dose cryo-HRTEM, XRD, and SEM measurements. D.T.B. and R.A.V. performed electrochemical measurements. P.S. performed NMR measurements. R.A.V. and Y.C. co-wrote the manuscript. All authors discussed the results and commented on the manuscript. **Competing interests:** The authors declare that they have no competing interests. **Data and materials availability:** All data needed to evaluate the conclusions in the paper are present in the paper and/or the Supplementary Materials.

Submitted 16 October 2022
Accepted 24 February 2023
Published 24 March 2023
10.1126/sciadv.adf3609